The Astrophysical Journal, 926:163 (13pp), 2022 February 20 https://doi.org/10.3847/1538-4357/ac4bbe

B-fields in Star-forming Region Observations (BISTRO): Magnetic Fields in the Filamentary Structures of Serpens Main

Woojin Kwon[1,2], Kate Pattle[3,4], Sarah Sadavoy[5], Charles L. H. Hull[6,7,91], Doug Johnstone[8,9], Derek Ward-Thompson[10], James Di Francesco[8,9], Patrick M. Koch[11], Ray Furuya[12,13], Yasuo Doi[14], Valentin J. M. Le Gouellec[15,16], Jihye Hwang[17,18], A-Ran Lyo[17], Archana Soam[19,15], Xindi Tang[20], Thiem Hoang[17,18], Florian Kirchschlager[3], Chakali Eswaraiah[21,22], Lapo Fanciullo[11], Kyoung Hee Kim[17], Takashi Onaka[23,24], Vera Könyves[10], Ji-hyun Kang[17], Chang Won Lee (이창원)[17,18], Motohide Tamura[24,25,26], Pierre Bastien[27], Tetsuo Hasegawa (長谷川哲夫)[26], Shih-Ping Lai[11,28], Keping Qiu[29,30], David Berry[31], Doris Arzoumanian[32], Tyler L. Bourke[33,34], Do-Young Byun[17,18], Wen Ping Chen[35], Huei-Ru Vivien Chen[11,28], Mike Chen[9], Zhiwei Chen[36], Tao-Chung Ching (慶道沖)[21,37], Jungyeon Cho[38], Yunhee Choi[17], Minho Choi[17], Antonio Chrysostomou[33], Eun Jung Chung[38], Simon Coudé[15], Sophia Dai[37], Pham Ngoc Diep[39], Yan Duan[37], Hao-Yuan Duan[28], David Eden[40], Jason Fiege[41], Laura M. Fissel[5], Erica Franzmann[41], Per Friberg[31], Rachel Friesen[42], Gary Fuller[43], Tim Gledhill[44], Sarah Graves[31], Jane Greaves[45], Matt Griffin[45], Qilao Gu[46], Ilseung Han[17,18], Jennifer Hatchell[47], Saeko Hayashi[48], Martin Houde[49], Tsuyoshi Inoue[50], Shu-ichiro Inutsuka[50], Kazunari Iwasaki[51], Il-Gyo Jeong[17,52], Miju Kang[17], Janik Karoly[10], Akimasa Kataoka[53], Koji Kawabata[54,55,56], Francisca Kemper[11,57], Kee-Tae Kim[17,18], Gwanjeong Kim[58], Mi-Ryang Kim[17], Shinyoung Kim[17,18], Jongsoo Kim[17,18], Jason Kirk[10], Masato I. N. Kobayashi[59], Takayoshi Kusune[59], Jungmi Kwon[24], Kevin Lacaille[60,61], Chi-Yan Law[46,62], Chin-Fei Lee[11], Yong-Hee Lee[31,63], Hyeseung Lee[38], Jeong-Eun Lee[63], Sang-Sung Lee[17,18], Dalei Li[64], Di Li[65,66], Hua-bai Li[46], Sheng-Jun Lin (林聖鈞)[28], Sheng-Yuan Liu[11], Hong-Li Liu[67], Junhao Liu (刘峻豪)[31], Tie Liu (刘铁)[68], Xing Lu[69], Steve Mairs[31], Masafumi Matsumura (松村雅文)[70], Brenda Matthews[8,9], Gerald Moriarty-Schieven[8], Tetsuya Nagata[71], Fumitaka Nakamura[53,72], Hiroyuki Nakanishi[73], Nguyen Bich Ngoc[39,74], Nagayoshi Ohashi[11], Geumsook Park[17], Harriet Parsons[31], Nicolas Peretto[45], Felix Priestley[45], Tae-Soo Pyo[48,72], Lei Qian[21], Ramprasad Rao[11], Jonathan Rawlings, Mark G. Rawlings[31,75], Brendan Retter[45], John Richer[76,77], Andrew Rigby[45], Hiro Saito[78], Giorgio Savini[79], Masumichi Seta[80], Yoshito Shimajiri[26,26], Hiroko Shinnaga[73], Mehrnoosh Tahani[81], Ya-Wen Tang[11], Kohji Tomisaka[53,72], Le Ngoc Tram[82], Yusuke Tsukamoto[73], Serena Viti[83], Hongchi Wang[36], Jia-Wei Wang[11], Anthony Whitworth[45], Jintai Wu[29], Jinjin Xie (謝津津)[37], Hsi-Wei Yen[11], Hyunju Yoo[17], Jinghua Yuan[37], Hyeong-Sik Yun[63], Tetsuya Zenko[71], Yapeng Zhang[84], Chuan-Peng Zhang[21,37], Guoyin Zhang[37], Jianjun Zhou[64], Lei Zhu[21], Ilse de Looze[83], Philippe André[85], C. Darren Dowell[86], Stewart Eyres[87], Sam Falle[88], Jean-François Robitaille[89], and Sven van Loo[90]

[1] Department of Earth Science Education, Seoul National University, 1 Gwanak-ro, Gwanak-gu, Seoul 08826, Republic of Korea; wkwon@snu.ac.kr
[2] SNU Astronomy Research Center, Seoul National University, 1 Gwanak-ro, Gwanak-gu, Seoul 08826, Republic of Korea
[3] Department of Physics and Astronomy, University College London, Gower Street, London WC1E 6BT, UK
[4] Centre for Astronomy, School of Physics, National University of Ireland Galway, University Road, Galway H91 TK33, Ireland
[5] Department for Physics, Engineering Physics and Astrophysics, Queen's University, Kingston, ON, K7L 3N6, Canada
[6] National Astronomical Observatory of Japan, Alonso de Córdova 3788, Office 61B, Vitacura, Santiago, Chile
[7] Joint ALMA Observatory, Alonso de Córdova 3107, Vitacura, Santiago, Chile
[8] NRC Herzberg Astronomy and Astrophysics, 5071 West Saanich Road, Victoria, BC V9E 2E7, Canada
[9] Department of Physics and Astronomy, University of Victoria, Victoria, BC V8W 2Y2, Canada
[10] Jeremiah Horrocks Institute, University of Central Lancashire, Preston PR1 2HE, UK
[11] Academia Sinica Institute of Astronomy and Astrophysics, No.1, Sec. 4., Roosevelt Road, Taipei 10617, Taiwan
[12] Tokushima University, Minami Jousanajima-machi 1-1, Tokushima 770-8502, Japan
[13] Institute of Liberal Arts and Sciences Tokushima University, Minami Jousanajima-machi 1-1, Tokushima 770-8502, Japan
[14] Department of Earth Science and Astronomy, Graduate School of Arts and Sciences, The University of Tokyo, 3-8-1 Komaba, Meguro, Tokyo 153–8902, Japan
[15] SOFIA Science Center, Universities Space Research Association, NASA Ames Research Center, Moffett Field, CA 94035, USA
[16] Université Paris-Saclay, CNRS, CEA, Astrophysique, Instrumentation et Modélisation de Paris-Saclay, F-91191 Gif-sur-Yvette, France
[17] Korea Astronomy and Space Science Institute, 776 Daedeokdae-ro, Yuseong-gu, Daejeon 34055, Republic of Korea
[18] University of Science and Technology, Korea, 217 Gajeong-ro, Yuseong-gu, Daejeon 34113, Republic of Korea
[19] Indian Institute of Astrophysics, II Block, Koramangala, Bengaluru 560034, India
[20] Xinjiang Astronomical Observatory, Chinese Academy of Sciences, 830011 Urumqi, People's Republic of China
[21] CAS Key Laboratory of FAST, National Astronomical Observatories, Chinese Academy of Sciences, People's Republic of China
[22] Indian Institute of Science Education and Research (IISER) Tirupati, Rami Reddy Nagar, Karakambadi Road, Mangalam (P.O.), Tirupati 517 507, India
[23] Department of Physics, Faculty of Science and Engineering, Meisei University, 2-1-1 Hodokubo, Hino, Tokyo 1191-8506, Japan
[24] Department of Astronomy, Graduate School of Science, The University of Tokyo, 7-3-1 Hongo, Bunkyo-ku, Tokyo 113-0033, Japan
[25] Astrobiology Center, National Institutes of Natural Sciences, 2-21-1 Osawa, Mitaka, Tokyo 181-8588, Japan
[26] National Astronomical Observatory of Japan, National Institutes of Natural Sciences, Osawa, Mitaka, Tokyo 181-8588, Japan
[27] Centre de recherche en astrophysique du Québec & département de physique, Université de Montréal, 1375, Avenue Thérèse-Lavoie-Roux, Montréal, QC, H2V 0B3, Canada
[28] Institute of Astronomy and Department of Physics, National Tsing Hua University, Hsinchu 30013, Taiwan
[29] School of Astronomy and Space Science, Nanjing University, 163 Xianlin Avenue, Nanjing 210023, People's Republic of China
[30] Key Laboratory of Modern Astronomy and Astrophysics (Nanjing University), Ministry of Education, Nanjing 210023, People's Republic of China
[31] East Asian Observatory, 660 N. A'ohōkū Place, University Park, Hilo, HI 96720, USA
[32] Aix Marseille Univ, CNRS, CNES, LAM, Marseille, France
[33] SKA Observatory, Jodrell Bank, Lower Withington, Macclesfield, SK11 9FT, UK

[34] Jodrell Bank Centre for Astrophysics, School of Physics and Astronomy, University of Manchester, Manchester, M13 9PL, UK
[35] Institute of Astronomy, National Central University, Zhongli 32001, Taiwan
[36] Purple Mountain Observatory, Chinese Academy of Sciences, 10 Yuanhua Road, 210023 Nanjing, People's Republic of China
[37] National Astronomical Observatories, Chinese Academy of Sciences, A20 Datun Road, Chaoyang District, Beijing 100012, People's Republic of China
[38] Department of Astronomy and Space Science, Chungnam National University, 99 Daehak-ro, Yuseong-gu, Daejeon 34134, Republic of Korea
[39] Vietnam National Space Center, Vietnam Academy of Science and Technology, 18 Hoang Quoc Viet, Hanoi, Vietnam
[40] Astrophysics Research Institute, Liverpool John Moores University, IC2, Liverpool Science Park, 146 Brownlow Hill, Liverpool L3 5RF, UK
[41] Department of Physics and Astronomy, The University of Manitoba, Winnipeg, Manitoba R3T2N2, Canada
[42] National Radio Astronomy Observatory, 520 Edgemont Road, Charlottesville, VA 22903, USA
[43] Jodrell Bank Centre for Astrophysics, School of Physics and Astronomy, University of Manchester, Oxford Road, Manchester M13 9PL, UK
[44] School of Physics, Astronomy & Mathematics, University of Hertfordshire, College Lane, Hatfield, Hertfordshire AL10 9AB, UK
[45] School of Physics and Astronomy, Cardiff University, The Parade, Cardiff CF24 3AA, UK
[46] Department of Physics, The Chinese University of Hong Kong, Shatin, N.T., Hong Kong, People's Republic of China
[47] Physics and Astronomy, University of Exeter, Stocker Road, Exeter EX4 4QL, UK
[48] Subaru Telescope, National Astronomical Observatory of Japan, 650 N. A'ohōkū Place, Hilo, HI 96720, USA
[49] Department of Physics and Astronomy, The University of Western Ontario, 1151 Richmond Street, London N6A 3K7, Canada
[50] Department of Physics, Graduate School of Science, Nagoya University, Furo-cho, Chikusa-ku, Nagoya 464-8602, Japan
[51] Department of Environmental Systems Science, Doshisha University, Tatara, Miyakodani 1-3, Kyotanabe, Kyoto 610-0394, Japan
[52] Department of Astronomy and Atmospheric Sciences, Kyungpook National University, Daegu 41566, Republic of Korea
[53] Division of Theoretical Astronomy, National Astronomical Observatory of Japan, Mitaka, Tokyo 181-8588, Japan
[54] Hiroshima Astrophysical Science Center, Hiroshima University, Kagamiyama 1-3-1, Higashi-Hiroshima, Hiroshima 739-8526, Japan
[55] Department of Physics, Hiroshima University, Kagamiyama 1-3-1, Higashi-Hiroshima, Hiroshima 739-8526, Japan
[56] Core Research for Energetic Universe (CORE-U), Hiroshima University, Kagamiyama 1-3-1, Higashi-Hiroshima, Hiroshima 739-8526, Japan
[57] European Southern Observatory, Karl-Schwarzschild-Str. 2, D-85748 Garching, Germany
[58] Nobeyama Radio Observatory, National Astronomical Observatory of Japan, National Institutes of Natural Sciences, Nobeyama, Minamimaki, Minamisaku, Nagano 384–1305, Japan
[59] Astronomical Institute, Graduate School of Science, Tohoku University, Aoba-ku, Sendai, Miyagi 980-8578, Japan
[60] Department of Physics and Astronomy, McMaster University, Hamilton, ON L8S 4M1 Canada
[61] Department of Physics and Atmospheric Science, Dalhousie University, Halifax B3H 4R2, Canada
[62] Department of Space, Earth & Environment, Chalmers University of Technology, SE-412 96 Gothenburg, Sweden
[63] School of Space Research, Kyung Hee University, 1732 Deogyeong-daero, Giheung-gu, Yongin-si, Gyeonggi-do 17104, Republic of Korea
[64] Xinjiang Astronomical Observatory, Chinese Academy of Sciences, 150 Science 1-Street, Urumqi 830011, Xinjiang, People's Republic of China
[65] CAS Key Laboratory of FAST, National Astronomical Observatories, Chinese Academy of Sciences, People's Republic of China
[66] University of Chinese Academy of Sciences, Beijing 100049, People's Republic of China
[67] Department of Astronomy, Yunnan University, Kunming, 650091, People's Republic of China
[68] Key Laboratory for Research in Galaxies and Cosmology, Shanghai Astronomical Observatory, Chinese Academy of Sciences, 80 Nandan Road, Shanghai 200030, People's Republic of China
[69] National Astronomical Observatory of Japan, Mitaka, Tokyo 181-8588, Japan
[70] Faculty of Education & Center for Educational Development and Support, Kagawa University, Saiwai-cho 1-1, Takamatsu, Kagawa, 760-8522, Japan
[71] Department of Astronomy, Graduate School of Science, Kyoto University, Sakyo-ku, Kyoto 606-8502, Japan
[72] SOKENDAI (The Graduate University for Advanced Studies), Hayama, Kanagawa 240-0193, Japan
[73] Department of Physics and Astronomy, Graduate School of Science and Engineering, Kagoshima University, 1-21-35 Korimoto, Kagoshima, Kagoshima 890-0065, Japan
[74] Graduate University of Science and Technology, Vietnam Academy of Science and Techonology, 18 Hoang Quoc Viet, Cau Giay, Hanoi, Vietnam
[75] Gemini Observatory, NSF's NOIRLab, 670 N. A'ohōkū Place, Hilo, HI 96720, USA
[76] Astrophysics Group, Cavendish Laboratory, J.J. Thomson Avenue, Cambridge CB3 0HE, UK
[77] Kavli Institute for Cosmology, Institute of Astronomy, University of Cambridge, Madingley Road, Cambridge, CB3 0HA, UK
[78] Faculty of Pure and Applied Sciences, University of Tsukuba, 1-1-1 Tennodai, Tsukuba, Ibaraki 305-8577, Japan
[79] OSL, Physics & Astronomy Dept., University College London, WC1E 6BT London, UK
[80] Department of Physics, School of Science and Technology, Kwansei Gakuin University, 2-1 Gakuen, Sanda, Hyogo 669-1337, Japan
[81] Dominion Radio Astrophysical Observatory, Herzberg Astronomy and Astrophysics Research Centre, National Research Council Canada, P.O. Box 248, Penticton, BC V2A 6J9, Canada
[82] University of Science and Technology of Hanoi, Vietnam Academy of Science and Technology, 18 Hoang Quoc Viet, Hanoi, Vietnam
[83] Physics & Astronomy Dept., University College London, WC1E 6BT London, UK
[84] Department of Astronomy, Beijing Normal University, Beijing 100875, People's Republic of China
[85] Laboratoire AIM CEA/DSM-CNRS-Université Paris Diderot, IRFU/Service d'Astrophysique, CEA Saclay, F-91191 Gif-sur-Yvette, France
[86] Jet Propulsion Laboratory, M/S 169-506, 4800 Oak Grove Drive, Pasadena, CA 91109, USA
[87] University of South Wales, Pontypridd, CF37 1DL, UK
[88] Department of Applied Mathematics, University of Leeds, Woodhouse Lane, Leeds LS2 9JT, UK
[89] Univ. Grenoble Alpes, CNRS, IPAG, F-38000 Grenoble, France
[90] School of Physics and Astronomy, University of Leeds, Woodhouse Lane, Leeds LS2 9JT, UK
Received 2021 March 10; revised 2021 December 23; accepted 2022 January 12; published 2022 February 22

Abstract

We present 850 μm polarimetric observations toward the Serpens Main molecular cloud obtained using the POL-2 polarimeter on the James Clerk Maxwell Telescope as part of the B-fields In STar-forming Region Observations

[91] NAOJ Fellow.

survey. These observations probe the magnetic field morphology of the Serpens Main molecular cloud on about 6000 au scales, which consists of cores and six filaments with different physical properties such as density and star formation activity. Using the histogram of relative orientation (HRO) technique, we find that magnetic fields are parallel to filaments in less-dense filamentary structures where $N_{H_2} < 0.93 \times 10^{22}$ cm^{-2} (magnetic fields perpendicular to density gradients), while they are perpendicular to filaments (magnetic fields parallel to density gradients) in dense filamentary structures with star formation activity. Moreover, applying the HRO technique to denser core regions, we find that magnetic field orientations change to become perpendicular to density gradients again at $N_{H_2} \approx 4.6 \times 10^{22}$ cm^{-2}. This can be interpreted as a signature of core formation. At $N_{H_2} \approx 16 \times 10^{22}$ cm^{-2}, magnetic fields change back to being parallel to density gradients once again, which can be understood to be due to magnetic fields being dragged in by infalling material. In addition, we estimate the magnetic field strengths of the filaments ($B_{POS} = 60$–$300\ \mu$G)) using the Davis–Chandrasekhar–Fermi method and discuss whether the filaments are gravitationally unstable based on magnetic field and turbulence energy densities.

Unified Astronomy Thesaurus concepts: Polarimetry (1278); Interstellar magnetic fields (845); Molecular clouds (1072); Submillimeter astronomy (1647); Interstellar medium (847); Interstellar filaments (842)

1. Introduction

Magnetic fields are thought to play a key role in various stages of star formation over a large range of scales. For example, ordered magnetic fields have been detected in molecular clouds on 0.1 pc and larger scales (e.g., Palmeirim et al. 2013; Li et al. 2014), suggesting that magnetic fields play a role in forming such structures. However, interferometric observations have shown that the magnetic fields of young stellar objects (YSOs) vary in morphology on about 100 au and smaller scales. Surveys of large samples of YSOs have reported that magnetic fields are randomly oriented with respect to bipolar outflows (e.g., Hull et al. 2013, 2014), while hourglass-shaped fields have been reported toward a few of the youngest protostellar systems (e.g., Girart et al. 2006; Stephens et al. 2013). Recent polarimetric observations made using the Atacama Large Millimeter/submillimeter Array have been revealing various detailed polarization and magnetic field structures on scales of 100 au and smaller toward many YSOs, with high angular resolution and sensitivity, including a clear hourglass morphology (e.g., Maury et al. 2018; Kwon et al. 2019), magnetic field structures tracing turbulence and/or outflow cavities (e.g., Hull et al. 2017; Sadavoy et al. 2018; Le Gouellec et al. 2019), and polarization patterns due to scattering of millimeter/submillimeter radiation by large grains (e.g., Cox et al. 2018; Lee et al. 2018; Sadavoy et al. 2019).

The B-fields In STar forming Region Observations (BISTRO) survey (Ward-Thompson et al. 2017) has been studying the role of magnetic fields in star formation at submillimeter wavelengths on about 2000–7000 au scales, using the James Clerk Maxwell Telescope (JCMT) and its polarimeter POL-2. This project began polarimetric observations in 2016 and was completed in early 2019, targeting 16 fields in nearby star-forming regions: e.g., Orion A (Pattle et al. 2017; Ward-Thompson et al. 2017; Hwang et al. 2021), Ophiuchus (Kwon et al. 2018; Soam et al. 2018; Liu et al. 2019; Pattle et al. 2019), IC 5146 (Wang et al. 2019), Barnard 1 (Coudé et al. 2019), NGC 1333 (Doi et al. 2020, 2021), Auriga (Bich Ngoc et al. 2021), L1689 (Pattle et al. 2021a), B213 (Eswaraiah et al. 2021), and NGC 2071IR (Lyo et al. 2021). In addition to studies of individual regions, Yen et al. (2021) found using all of the BISTRO data that magnetic fields are misaligned with outflows by about 50° on 0.05–0.5 pc scales. The BISTRO project was extended to include more distant and more massive star-forming regions (BISTRO-2; Pattle et al. 2018; Arzoumanian et al. 2021; Könyves et al. 2021) and to observe a wider range of evolutionary stages and star formation environments (BISTRO-3).

As part of the BISTRO survey, this paper focuses on the Serpens Main molecular cloud, which is located at a distance of 415 pc (Dzib et al. 2010; Herczeg et al. 2019). Serpens Main consists of two subclusters—northwest (hereafter NW) and southeast (SE)—and has largely been studied as an active, intermediate-mass star-forming region. For example, several tens of YSOs have been detected in the region by the Spitzer Space Telescope (Harvey et al. 2007; Evans et al. 2009), and it was found that younger YSOs (Class 0/I) are located in the central regions of the subclusters, while older YSOs (Class II/III) are more widely distributed, and preferentially located in the SE subcluster (Winston et al. 2007). Furthermore, the SE subcluster shows larger velocity gradients compared to the NW subcluster (Graves et al. 2010). Lee et al. (2014) mapped the molecular cloud at 7″ resolution in the 3 mm continuum and the N_2H^+, HCO^+, and HCN (1–0) molecular lines, using the Combined Array for Research in Millimeter-wave Astronomy (CARMA). They identified six filamentary structures using the N_2H^+ (1–0) channel maps. Interestingly, two filaments are less dense and do not have star formation activity, while the others are dense enough for gravitational collapse and/or have YSOs. The properties of, and star formation activity within, these filaments need to be investigated alongside their magnetic fields, and are the main topics of this paper. Previously, Matthews et al. (2009) detected linear polarizations toward Serpens Main using the JCMT and SCUPOL (the predecessor to POL-2), but the polarized signal was detected only in limited regions in the centers of the two subclusters, which made it impossible to study the magnetic fields in the filamentary structures. Conversely, Sugitani et al. (2010) have studied the large-scale magnetic fields around the molecular cloud using near-infrared imaging polarimetry. The detailed magnetic fields within the molecular cloud, however, could not be studied using such data.

In this paper, we describe how the data have been taken and reduced in Section 2. Detected polarization measurements and inferred magnetic fields are introduced in Section 3, followed by discussions on the relationships between the physical properties of the filaments, including their magnetic fields and star formation activities (Section 4). We address the column densities at which the relative directions of magnetic fields and column density structures change, in Section 4. Finally, we summarize our results in Section 5.

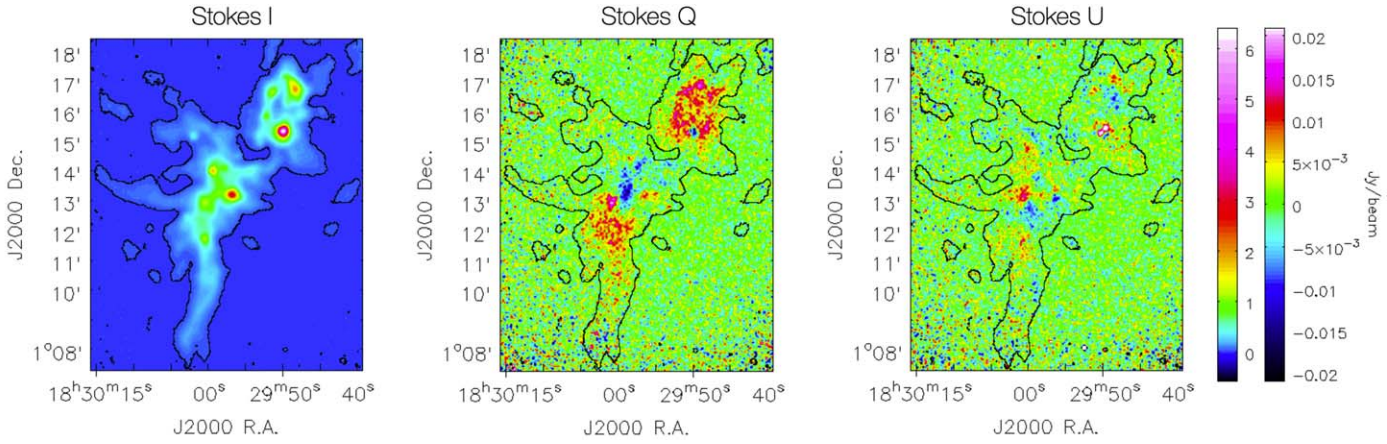

Figure 1. Stokes I, Q, and U maps (left, center, and right, respectively) toward the Serpens Main molecular cloud obtained at 850 μm using JCMT/POL-2 as part of the BISTRO survey. The contours indicate 12 mJy beam^{-1} in the total intensity map, which is approximately at the 3σ level.

2. Observations

We observed the Serpens Main molecular cloud using the 15 m diameter JCMT, as part of the BISTRO survey. The POL-2 polarimeter was inserted into the ray pathway of the Submillimeter Common-User Bolometer Array 2 (SCUBA-2; Holland et al. 2013) camera, in order to make linear polarization measurements. Both 450 and 850 μm measurements are taken simultaneously, but only the 850 μm data, with an angular resolution of 14″, are used in this study. POL-2 observations adopt a modified version of the standard SCUBA-2 Daisy pattern, scanning the sky at a speed of 8″ s^{-1} with a half-wave plate rotation speed of 2 Hz. This mode allows each 4″ pixel to contain samples from a full revolution of the half-wave plate (Friberg et al. 2016), and provides 13′ diameter mapping coverage with a central 3 arcminute-diameter area of the best sensitivity. Two pointings have been observed, each for 14 hr (21 repeats of 40 minute long observing blocks) in JCMT weather band 2 ($0.05 < \tau < 0.08$ at 225 GHz), in order to cover the whole Serpens Main molecular cloud to good sensitivity. The two pointings were centered on (R.A., decl.) = (18:29:59.370, +01:12:52.00) and (18:29:49.530, +01:16:11.10) in J2000 coordinates for the southeast (SE) and the northwest (NW) fields, respectively. The SE field was observed in 2016 April–May, while the NW field was observed in 2017 March–May.

Standard POL-2 data reduction procedures were followed using the *pol2map*[92] routine, which has recently been added to the *Starlink* software suite (Currie et al. 2014). The *pol2map* routine makes Stokes I (total intensity), Stokes Q, and Stokes U maps from POL-2 time-stream data. At the final stage of making images using *pol2map*, the *skyloop*[93] algorithm, an implementation of the SCUBA-2 iterative mapmaking algorithm *makemap* (Chapin et al. 2013), which improves image consistency by reducing multiple observations simultaneously, was used. We applied the "2019 August" instrumental polarization (IP) model[94] to the data, with our final total intensity map serving as the model for estimating artificial polarized emission to be corrected for. In addition to the typical POL-2 procedures (e.g., Pattle et al. 2021a), additional steps were taken to combine the SE and NW fields. Data from the two pointings were initially reduced separately to make initial total intensity maps. These maps were combined to produce an initial co-added total intensity map, which was used to generate a signal-to-noise-based mosaic mask for use in the next step. This mask constrains the mapmaker by defining a fixed area containing an astrophysical signal (Chapin et al. 2013). The data from each field were again reduced separately, at this stage invoking the *skyloop* algorithm and using the mask defined based on the initial co-added *I* map, to generate Stokes *Q* and *U* maps, and an improved Stokes *I* map. The *Q* and *U* maps were corrected for instrumental polarization using the improved Stokes *I* map and the 2019 August IP model. Finally, the maps of the two fields were co-added, to produce a final mosaicked set of Stokes *I*, *Q*, and *U* maps from which polarization fractions and directions were calculated using the equations: $p = PI/I$ and $\psi = 0.5\tan^{-1}(U/Q)$, where p is polarization fraction and PI is polarized intensity. When calculating the polarization intensities, classical de-biasing was adopted, such that $PI = \sqrt{Q^2 + U^2 - \sigma^2}$, where $\sigma^2 = (Q^2\sigma_Q^2 + U^2\sigma_U^2)/(Q^2 + U^2)$. Finally, the raw POL-2 power unit of pW was converted to intensity units of Jy beam^{-1} using the POL-2 flux conversion factor (FCF) of 725 Jy beam^{-1} pW^{-1}, determined by multiplying the SCUBA-2 850 μm FCF (537 Jy beam^{-1} pW^{-1}; Dempsey et al. 2013) by a factor 1.35 to account for additional losses in POL-2 at 850 μm (Friberg et al. 2016). All of the maps were made using the default 4″ pixels, and the noise level achieved in the final total intensity map is about 4 mJy beam^{-1}.

3. Results

Figure 1 shows our Stokes I, Q, and U maps, demonstrating linear polarization signal toward Serpens Main. The noise levels achieved are 3.8, 3.1, and 2.9 mJy beam^{-1}, respectively. As shown in the figure, linear polarizations have been detected well over a large region, not only in the centers of the two subclusters. Previous JCMT/SCUPOL observations also detected a clear linear polarization signal, but these detections were limited to only the central regions (Matthews et al. 2009) due to lack of sensitivity.

The Serpens Main molecular cloud has six filamentary structures located predominantly in the SE subcluster, as shown in the inset panel of Figure 2. Lee et al. (2014) observed Serpens Main in the 3 mm continuum and three J = 1–0 molecular lines of N_2H^+, HCO^+, and HCN using CARMA at

[92] http://starlink.eao.hawaii.edu/docs/sc22.htx/sc22.html
[93] http://starlink.eao.hawaii.edu/docs/sun258.htx/sun258ss72.html
[94] https://www.eaobservatory.org/jcmt/2019/08/new-ip-models-for-pol2-data/

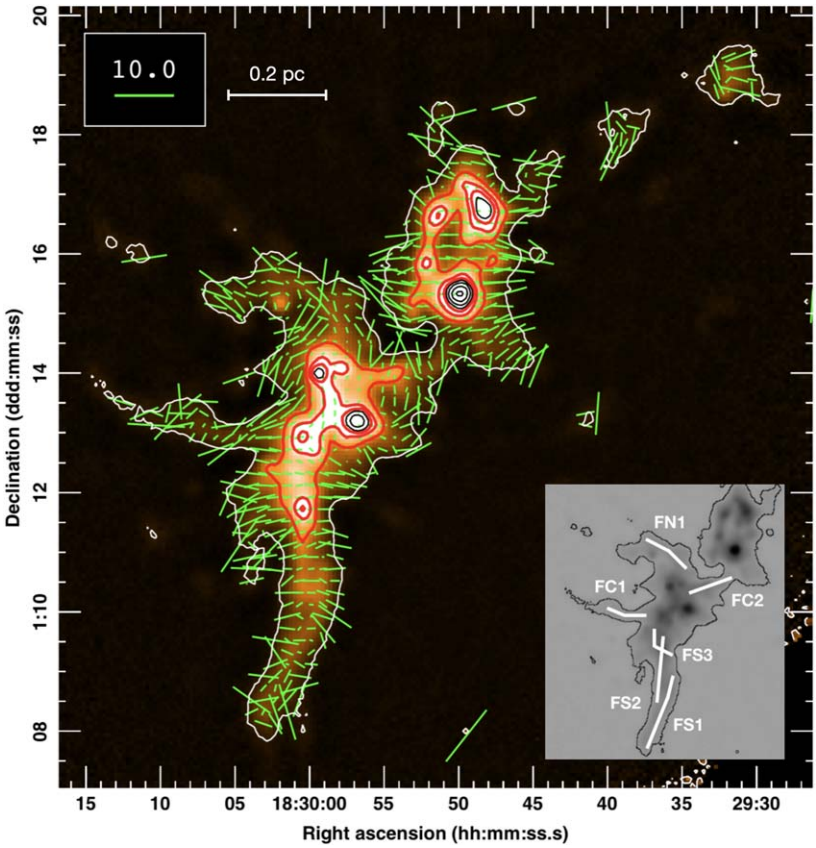

Figure 2. Serpens Main magnetic field directions (green segments) inferred from 850 μm JCMT POL-2 observations by rotating polarization directions by 90°. The green segment lengths indicate polarization fractions; a polarization fraction of 10% is shown by the bar at the top left. The white bar indicates a length scale at 415 pc, the distance of Serpens Main. The color scale and contours show the total intensity distribution. Contour levels are 0.042, 0.362, 0.725, 1.090, 1.450, 2.170, 3.620, and 5.800 Jy beam^{-1}. The inset panel identifies the six filaments discussed in the text.

Table 1
Selected Physical Properties of Filaments

Filament	Width (pc)	∇V (km s^{-1} pc^{-1})	$\langle\sigma\rangle$ (km s^{-1})	$\langle\sigma\rangle_{\rm nt}$ (km s^{-1})	N_{H_2} ($\times10^{22}$ cm^{-2})	Mass ($M_\odot$)	M_L ($M_\odot$ pc^{-1})	$M_{L,\rm crit}$ ($M_\odot$ pc^{-1})	YSOs
FN1	0.03	3.2 ± 0.08	0.27	0.21	3.6	3.79	18.0	23.7	no
FC1	0.04	4.8 ± 0.14	0.25	0.24	3.5	4.76	28.0	20.0	no
FC2	0.05	0.7 ± 0.07	0.21	0.20	5.2	10.57	52.9	22.4	no
FS1	0.04	0.8 ± 0.03	0.13	0.12	4.3	16.33	49.5	19.2	yes
FS2	0.03	1.5 ± 0.08	0.24	0.23	7.9	17.95	74.8	20.2	yes
FS3	0.03	0.8 ± 0.07	0.23	0.22	9.3	14.08	82.8	20.5	yes

Note. All of the values and information in this table come from Lee et al. (2014), who identified the filaments using CARMA N_2H^+ (1–0) observations with an angular resolution of 7″. The columns list filament widths, velocity gradients along the filaments (∇V), velocity dispersions ($\langle\sigma\rangle$), nonthermal velocity dispersions ($\langle\sigma\rangle_{\rm nt}$), column densities of molecular hydrogen (N_{H_2}), filament masses, filament masses per length (M_L), critical filament masses per length ($M_{L,\rm crit}$), and whether YSOs are found.

7″ resolution. They analyzed its structures and kinematics using the dendrogram technique (Rosolowsky et al. 2008). In particular, they identified six filamentary structures based on the integrated intensity and channel maps of N_2H^+ (1–0), which is known to trace high-density regions: e.g., $n_{\rm crit}(N_2H^+$ 1–0$) = 6.1 \times 10^4$ cm^{-3} at $T = 10$ K (Shirley 2015). Some properties of the filaments selected from Lee et al. (2014) are listed in Table 1, and refer to the filaments identified in the inset panel of Figure 2. Note that there are two types of filaments: (i) FN1, FC1, and FC2 have no YSOs, while (ii) the other three filaments contain YSOs. Furthermore, filaments FN1 and FC1 are less dense and have large velocity gradients, while the other filaments are denser and have relatively small velocity gradients. Finally, the linear densities of the FN1 and FC1 filaments are comparable to or lower than the critical values for isothermal, self-gravitating cylinders without magnetic support, above which they can gravitationally contract (Ostriker 1964; Lee et al. 2014).

3.1. Field Morphology

Magnetic fields, and specifically the field morphology projected on the plane of sky, can be studied using polarized thermal emission from dust grains. Nonspherical dust grains spin around their minor axes due to radiative anisotropic torques. Within a magnetic field, such spinning grains will have

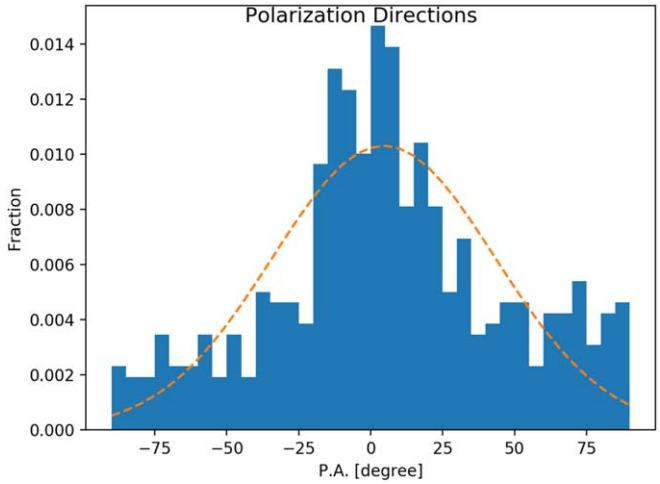

Figure 3. A histogram of polarization position angles (P.A.s) in Serpens Main. The orange dashed line shows a Gaussian fit to the histogram, with $\bar{\theta} = 4.^{\circ}5$ and $\sigma = 38.^{\circ}7$.

their minor axes aligned parallel to the field (e.g., Lazarian & Hoang 2007). Therefore, the thermal emission of nonspherical dust grains is linearly polarized perpendicular to the field. This allows us to infer magnetic field directions by rotating linear polarization angle measurements by 90°. Note that in contrast, at short wavelengths such as those in the optical regime, polarization is mainly caused by preferential absorption of unpolarized background emission by aligned grains, rather than by the emission from grains. Thus, at those shorter wavelengths, linear polarization and magnetic field directions are parallel to one another.

Figure 2 shows magnetic field directions projected onto the plane of sky across Serpens Main as green segments, inferred by rotating the linear polarization angles by 90°, overlaid on the 850 μm total intensity map. Data points with a signal-to-noise ratio (S/N) in total intensity of greater than 30 and a polarization fraction smaller than 15% have been selected after binning up by a factor of 3 in pixel width. This binning yields a pixel size of 12″, comparable to the angular resolution of $\sim 14''$. The lengths of the segments indicate polarization fractions, which are relatively large (up to about 10%) in the low-intensity boundary regions, and get smaller going into the dense core regions. The polarization fractions are discussed quantitatively in the next subsection.

The distribution of polarization directions is shown as a histogram in Figure 3. The most common direction is P.A. $= 4.^{\circ}5$, suggesting that an east–west magnetic field dominates. This direction is somewhat consistent with that measured by Planck toward Serpens Main. We estimate an average direction of P.A. $= -20^{\circ}$ from the Planck polarimetric data at 353 GHz (Planck Collaboration et al. 2016), assuming a 10′ beam at the J2000 center position of Serpens Main, (R.A., decl.) = (18:29:55, +01:13:00). Since the histogram shown in Figure 3 is a distribution of polarization angles measured on smaller scales than those of the Planck data, the means of the directions are not expected to agree entirely, and the difference of $\sim 25^{\circ}$ can be understood. The polarization direction of Planck data matches the direction of elongation of the Serpens Main molecular cloud, suggesting that the large-scale magnetic field is perpendicular to the overall elongation of the molecular gas structures. This large-scale field has also been reported in near-infrared polarimetric observations sensitive to the periphery of the molecular cloud (Sugitani et al. 2010).

The magnetic field directions within individual filaments with differing physical properties are one of the key focuses of this study. Figure 2 shows that the southern filaments, FS1, FS2, and FS3, have magnetic fields preferentially oriented in the east–west direction. This trend suggests that the field directions are perpendicular to these filaments overall at the angular resolution of our data, which is too low to separate FS2 and FS3. A similar behavior is observed in the FC2 region. In contrast, the FN1 and FC1 filaments exhibit field directions that are mainly parallel to their major axes. Since FN1 and FC1 are less dense than the other filaments, this difference suggests that magnetic fields are parallel to filaments in less-dense cases but perpendicular in denser ones, a result that has been reported in many previous studies (e.g., Planck Collaboration et al. 2016; Ward-Thompson et al. 2017). However, magnetic field directions change dramatically at the locations of dense cores. For example, the magnetic field seems to surround the core located to the south of FN1, (R.A., decl.) = (18:30:02, +01:15:10). Field direction variations are also clearly seen in the central core regions of both the NW and SE subclusters. A detailed quantitative analysis and discussion of the relative orientations of magnetic fields with respect to the filaments follow in Section 4. Comparisons between the magnetic field on the scales resolved in these data and in interferometric observations of Serpens Main will be undertaken in a separate paper (Y.-W. Tang et al. 2022, in preparation).

3.2. Polarization Fraction as a Function of Continuum Intensity

The relationship between polarization fraction and column density (or continuum intensity as a proxy for column density) has been used to show where polarized dust emission originates from in star-forming clouds. Polarization fractions depend on both grain properties and local physical conditions (Andersson et al. 2015). In the case of linear polarization of dust thermal emission that is used in this study, there must be a mechanism by which nonspherical dust grains are aligned. Such mechanisms include anisotropic radiation, subsonic or supersonic flows, and/or magnetic fields. In the relevant case of the interstellar medium and molecular clouds whose dust grains are still submicrometer to several micrometers in size, polarization principally arises from spinning dust grains, which are aligned with respect to the magnetic field by torques from an incident anisotropic radiation field; i.e., both a magnetic field and an incident radiation field are needed.

Figure 4 presents the relationship between polarization fraction and continuum intensity in Serpens Main at 850 μm on a log–log scale. Only data points that have an S/N in total intensity larger than 30 and a polarization fraction smaller than 15% have been selected. The black dashed line denotes a slope of −1 for reference, i.e., $p \propto I^{-1}$. The blue and red solid lines show the trend of the highest polarization data points at each intensity ($p \propto I^{-0.8}$; i.e., the behavior of the upper envelope of the data points) and the result of fitting a power law to the full sample ($p = 75.6\, I^{-0.634}$), respectively. Note that the slopes of both the upper-envelope trend and the fit are shallower than −1. If polarization were limited to the outer shell area of the molecular cloud, the relationship between polarization fraction and intensity would follow the reference slope of −1 (e.g., Jones et al. 2015). The data points in Serpens Main, however, show a shallow slope, so polarization is

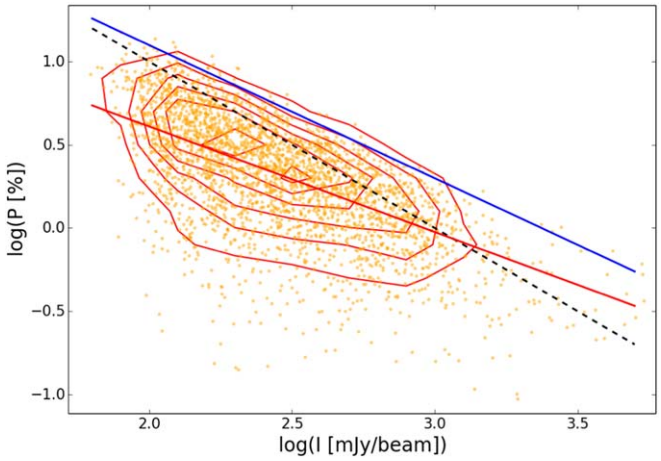

Figure 4. The relationship between polarization fraction and total intensity in Serpens Main. The black dashed, blue solid, and red solid lines denote slopes of −1, −0.8, and −0.634, respectively.

not limited to the periphery of the molecular cloud; some must originate from the dense inner regions of the cloud as well. This overall trend of polarization fraction decreasing with intensity is well known, and often found in molecular clouds (e.g., Kwon et al. 2018; Soam et al. 2018; Coudé et al. 2019; Liu et al. 2019; Pattle et al. 2019; Wang et al. 2019). This trend is understood to result from weakening of dust grain alignment mechanisms in high-density regions, due to decreasing radiation fields and increasing gas density and grain sizes (e.g., Hoang et al. 2021). In addition, varying magnetic field directions along the line of sight depolarize the signal, due to integration over multiple magnetic field components. Studies of alternative polarization mechanisms and dust properties, which are also interesting and important, have been carried out (e.g., Planck Collaboration et al. 2020; Le Gouellec et al. 2020; Pattle et al. 2021b), but are unlikely to apply on the size scales that we consider.

We note that Pattle et al. (2019) showed that as polarization intensities are calculated using the squared sum of Stokes Q and U values, resulting in the noise characteristics of polarization fractions following a Ricean distribution, an observed power-law index of −1 of polarization fraction as a function of intensity may result from the non-detection of polarized emission, raising the need for caution when interpreting such a relationship. Our results, however, clearly show a shallower power-law index, indicating real detections. Note that in the regime with a power-law index slope shallower than −1, i.e., well-detected polarization, both the Rice distribution and the power-law approaches are consistent with one another.

4. Discussion

4.1. Histogram of Relative Orientations

The relationship between magnetic fields and filamentary structures can be studied quantitatively using the histogram of relative orientations (HRO) technique (Soler et al. 2013; Planck Collaboration et al. 2016), which compares polarization directions ($\hat{E}$) against optical depth gradients ($\nabla\tau$). For the HRO technique, a histogram of relative orientations (ϕ) between $\hat{E}$ and $\nabla\tau$ needs to be produced at each density to be investigated. In this work, instead of using optical depth gradients, we use intensity gradients for simplicity, which is reasonable in a small region where temperatures and dust properties are not varying significantly. Note that in the optically thin regime, which is our case, intensity is proportional to the product of the Planck function for blackbody radiation and the optical depth. Thus, a 15% variation of temperature, e.g., between 12 and 14 K, produces a 25% variation in intensity at 850 μm. In addition, note that the directions of the gradients are analyzed here, not the amplitudes of the gradients. Next, within the HRO, the central area (A_c, where $|\phi| < 22.^{\circ}5$) and the extreme area (A_e, where $|\phi| > 67.^{\circ}5$) are calculated. Finally, the histogram shape parameter (ξ) is calculated:

$$\xi = \frac{A_c - A_e}{A_c + A_e}. \quad (1)$$

When the relative orientation of most data points is small, i.e., when polarization directions are parallel to optical depth (here intensity) gradients, ξ is positive since $A_c > A_e$. In contrast, when polarizations are perpendicular to intensity gradients, ξ is negative. Since the magnetic field direction is perpendicular to the polarization and the filament direction is perpendicular to the intensity gradient, positive values of the histogram shape parameter ξ also imply that magnetic fields are parallel to filaments. In the same way, negative ξ values indicate that magnetic fields are perpendicular to filaments. The uncertainties on ξ are dominated by the number of data points in each bin of the histogram and are calculated as (Planck Collaboration et al. 2016)

$$\sigma_\xi^2 = \frac{4(A_e^2\sigma_{A_c}^2 + A_c^2\sigma_{A_e}^2)}{(A_c + A_e)^4}. \quad (2)$$

Here, σ_{A_c} and σ_{A_e} are obtained following $\sigma_k^2 = h_k(1 - h_k/h_{\rm tot})$, where h_k corresponds to the number of data points in the central or extreme bin, and $h_{\rm tot}$ is the total number of data points.

Figure 5 presents the histogram shape parameters for individual filaments as well as for all filaments combined. The data used for the plot are gridded to 4″ pixels, with an S/N in total intensity larger than 3, an S/N in polarized intensity larger than 2, a polarization angle uncertainty smaller than 15°, and a polarization fraction smaller than 15%. Data points for individual filament areas have been selected by eye based on the identifications of Lee et al. (2014) and are presented in the left panel of Figure 5. Note that the main trends of the HRO analysis do not change depending on whether a few segments are included or excluded. The column densities ($N_{\rm H_2}$) of molecular hydrogen used in this analysis are calculated from the 850 μm dust thermal intensities (I_ν):

$$N_{\rm H_2} = \frac{I_\nu}{\kappa_\nu B_\nu(T_d)\,\mu_{\rm H_2} m_{\rm H}\Omega}, \quad (3)$$

where κ_ν is the mass absorption coefficient at 850 μm assuming a gas-to-dust mass ratio of 100 (0.02 cm^2 g^{-1}), T_d is the dust temperature (12 K; Lee et al. 2014), $\mu_{\rm H_2}$ is the molecular weight per hydrogen molecule (2.8; Kauffmann et al. 2008), $m_{\rm H}$ is the atomic hydrogen mass (1.67×10^{-24} g), and Ω is the beam solid angle.

As shown in Figure 5 by the black solid line, the ξ values using all filament data decrease with column density. The transition from positive to negative ξ is not clear, since it happens in the first bin where the mean intensity corresponds to $N_{\rm H_2} \approx 0.93 \times 10^{22}$cm^{-2}. Therefore, although individual filaments reveal a range of properties, which are addressed below, the overall transition of the magnetic field from parallel to

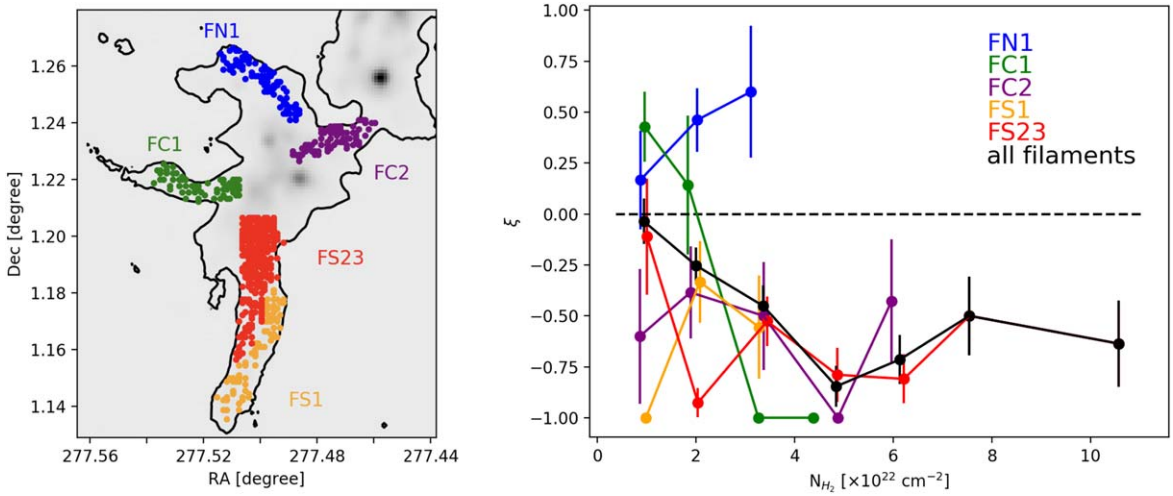

Figure 5. The left panel shows individual filament regions (Lee et al. 2014) used in the HRO analysis, and the black contour indicates a level of 0.042 Jy beam^{-1}. The right panel shows the histogram shape parameter (ξ) for these filaments, with the black line indicating the result using all filaments combined.

perpendicular within the Serpens Main filaments tends to occur around this column density.

Individual filaments show a range of relative orientations for their associated magnetic fields, as shown in various colors in Figure 5. First, all of the histogram shape parameters of the filament FN1 are positive (blue), which means that the magnetic fields in FN1 are parallel to the filamentary structure. Also, note that FN1 is the least-dense filament, $N_{\rm H_2} < 3.1 \times 10^{22}$ cm^{-2}. Next, FC1 is the second least-dense filament and shows a transition from positive to negative ξ values (green), which indicates that magnetic fields are parallel to the filament in its less-dense regions but perpendicular in the relatively denser regions. Note that the mass-per-length values of these two filaments are subcritical (FN1) or marginally supercritical (FC1) even without considering magnetic fields, and they have no embedded YSOs (Table 1). All of the other filaments (FC2, FS1, and FS2/3) have negative ξ values, suggesting that their magnetic fields are perpendicular to their major axes. Filaments FS2 and FS3 are not easy to separate from each other, so we consider them together. Indeed, these two filaments are very similar in density as the densest filaments among the sample (Table 1). We also note that there is no significant magnetic field variation over the region in response to the different observed filament directions.

This trend of relative magnetic field orientation changing with density has been reported in multiple previous studies. For example, Planck Collaboration et al. (2016) examined the relative orientations between magnetic field directions and column density structures by applying the HRO technique to Planck polarimetric data at 353 GHz. Those authors found that a transition from parallel to perpendicular orientations appears between $N_{\rm H} \sim 0.5 \times 10^{22}$ cm^{-2} and $\sim 5 \times 10^{22}$ cm^{-2}, consistent with our result above.

We further investigated the magnetic field orientation by applying the HRO analysis to all of the dense region observations. Figure 6 shows the histogram shape parameters (ξ) calculated from the whole of Serpens Main including the central subcluster areas as well as the filamentary structures. In the figure, the regime with a column density less than $N_{\rm H_2} \sim 4.6 \times 10^{22}$ cm^{-2} is mainly that of the filamentary structures, in which the ξ values decrease with density. Between $N_{\rm H_2} \sim 4.6 \times 10^{22}$ and $\sim 10 \times 10^{22}$ cm^{-2}, however, the ξ values increase up to zero. This increase suggests that the magnetic fields are trending parallel to elongated structures around a column density of $N_{\rm H_2} \sim 10 \times 10^{22}$ cm^{-2}. In other words, magnetic fields become perpendicular to density gradients (where elongated spines are defined as being orthogonal to the direction of a density gradient). The transition can be understood as a result of the local density gradients becoming more significant than the initial density gradients across filaments, presumably arising from mass accumulation of neutral species crossing magnetic field lines (ambipolar diffusion; e.g., Mouschovias 1979; Hennebelle & Inutsuka 2019). Also, this regime corresponds to the area where filaments transition into the central hub while maintaining their initial perpendicular fields. With increasing density, the ξ values again decrease and get back to the overall decreasing trend around $N_{\rm H_2} \sim 16 \times 10^{22}$ cm^{-2}, which indicates that magnetic fields are again parallel to density gradients (i.e., perpendicular to "filaments"). This behavior can be understood as magnetic field lines now being dragged along by gravitational collapse at these high column densities.

The HRO analysis toward the Serpens Main molecular cloud nicely shows the three transitional boundaries in column density for relative orientations of magnetic fields with respect to the physical structures of filaments and cores. Figure 7 summarizes the four column density regimes within the Serpens Main molecular cloud as a schematic diagram. First, magnetic fields are parallel to the least-dense filaments, particularly where $N_{\rm H_2} \lesssim 0.93 \times 10^{22}$ cm^{-2} (region 1). This column density threshold corresponds to $n(H_2) \approx 1.0 \times 10^5$ cm^{-3}, assuming a 0.03 pc filament width. In contrast, denser filaments ranging from $0.93 \times 10^{22} < N_{\rm H_2} \lesssim 4.6 \times 10^{22}$ cm^{-2} have magnetic fields perpendicular to their filamentary structure (region 2). Where the column density becomes larger than $N_{\rm H_2} \sim 4.6 \times 10^{22}$ cm^{-2}, cores form and a significant density gradient along a filament appears (region 3). This column density corresponds to $n(H_2) \approx 5.0 \times 10^5$ cm^{-3}, assuming cores of about 0.03 pc in size. Note that assuming a filament width of 0.03 pc, the critical mass per length $M_{L,\rm crit} = 20\,M_\odot$ pc^{-1} corresponds to $N_{\rm H_2} = 3.0 \times 10^{22}$ cm^{-2}. Considering the presence of magnetic fields, it is interesting that the column density associated with cores in Serpens Main is larger than this

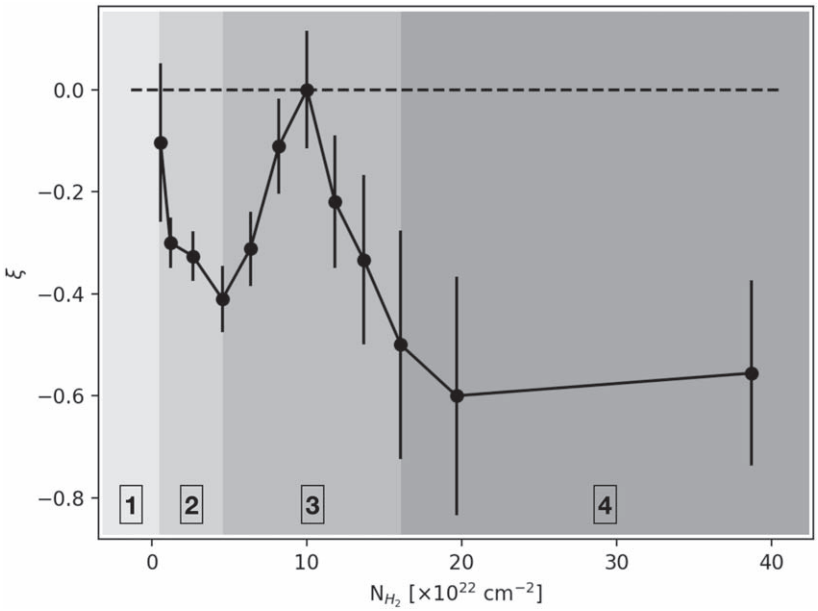

Figure 6. Histogram shape parameters (ξ) of the Serpens Main molecular cloud including both the filament and the core regions. Note that the least-dense regions have an almost positive value of ξ, and there is a bump at moderate column density: ξ becoming positive and decreasing again. Refer to the text for discussion. The region numbers correspond to those in Figure 7 and in the text.

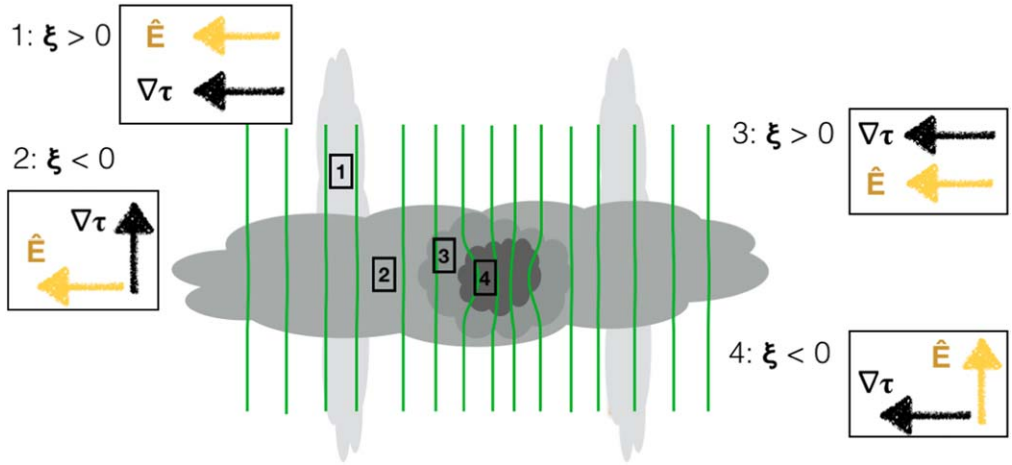

Figure 7. Schematic diagram showing four regions with different relationships between the magnetic field and density gradient. Note that the green lines are magnetic field lines, and the darker gray colors indicate denser regions. The yellow vectors are polarization directions that are perpendicular to the magnetic field lines, and the black vectors are optical depth gradients that correspond to density gradients. The four regions are (1) less-dense filaments, (2) dense filaments, (3) core-forming regions, and (4) regions in which the field is dragged in.

value. Finally, at column densities above $N_{\rm H_2} \sim 16 \times 10^{22}$ cm^{-2}, magnetic fields are also dragged in by frequent collisions between charged and neutral species during the dynamical contraction, resulting in magnetic fields that are again parallel to the density gradient (region 4). When assuming the same size scale for cores as previously (0.03 pc), this column density threshold corresponds to $n(H_2) \approx 18 \times 10^5$ cm^{-3} or higher.

In addition to the transition of magnetic field relative orientations between less-dense and more-dense filamentary structures, this further transition occurring at a higher density, which we recover, has recently been reported by multiple other studies. Pillai et al. (2020) showed that magnetic fields become parallel to filaments at a visual extinction $A_v \approx 20$–30 magnitude in the Serpens South cloud. That extinction is equivalent to $N_{\rm H} \approx 4.5 \times 10^{22}$–$6.6 \times 10^{22}$ cm^{-2} ($N_{\rm H_2} \approx 1.6 \times 10^{22}$–$2.4 \times 10^{22}$ cm^{-2}), based on the relation between visual extinction and column density (Güver & Özel 2009). Although their column density threshold differs from ours by a factor of 2, the transition likely corresponds with our boundary between regions 2 and 3 (Figure 7). Also, Wang et al. (2020) found that the filament and hub system G33.92+0.11 has a magnetic field parallel to the gravity vector and the gas motion within the central hub region. Since a gravity direction is comparable to a density gradient, it appears that the hub region corresponds to region 4 of our scenario.

4.2. Field Strength and Star Formation

Magnetic field strength, specifically the component projected on the plane of the sky, can be estimated from linearly polarized dust thermal emission using the Davis–Chandrasekhar–Fermi (DCF) method (Davis 1951; Chandrasekhar & Fermi 1953). The DCF method estimates a field strength at a given gas density and

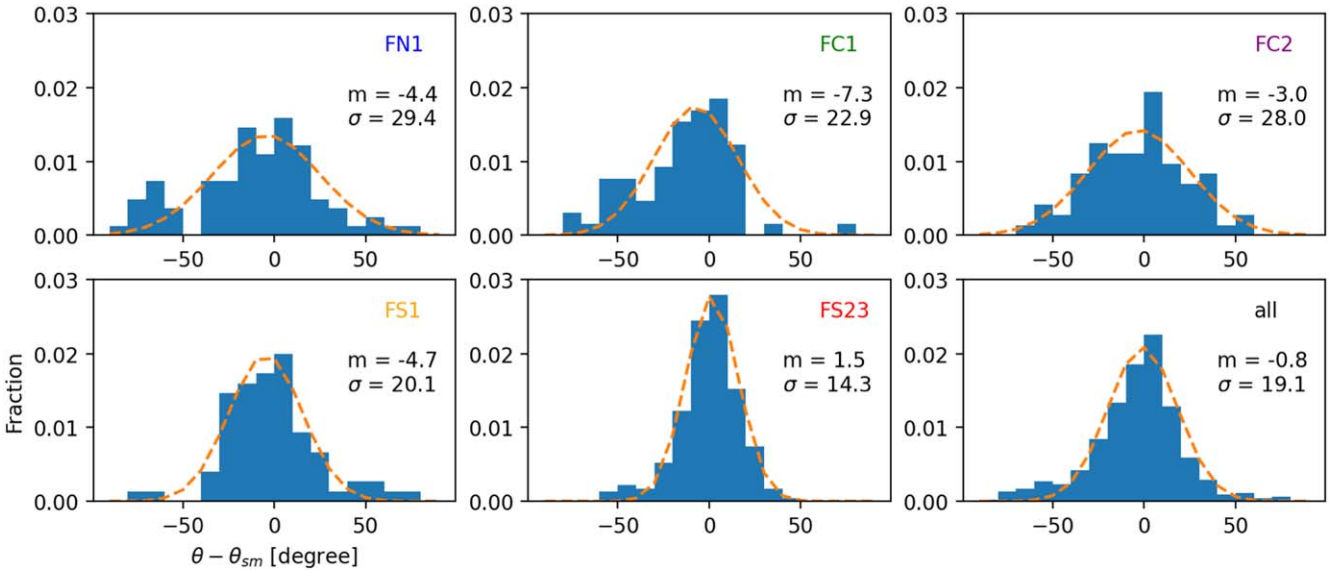

Figure 8. Magnetic field dispersion for individual filaments and all filaments combined. In each panel, the horizontal axis is position-angle difference in degrees between the magnetic field direction of the non-smoothed and smoothed data. The orange dashed lines are Gaussian functions fitted to the histograms, whose mean and standard deviation values are listed in the panels.

Table 2
Magnetic Field Strength Measures for Filaments

Filament	N_{H_2} ($\times 10^{22}$ cm^{-2})	$n(H_2)$ ($\times 10^5$ cm^{-3})	$\delta\,\phi$ (deg)	B_{POS} (μG)	λ	$P_{B_{POS}}$ ($\times 10^{-10}$ erg cm^{-3})	P_{turb} ($\times 10^{-10}$ erg cm^{-3})	$M_L/M_{L,crit}$
FN1	2.6	2.8	29.4	83 ± 35	2.4 ± 1.6	2.73	6.21	0.76
FC1	2.2	1.8	22.9	97 ± 32	1.7 ± 1.0	3.74	5.14	1.4
FC2	4.4	2.9	28.0	84 ± 26	4.0 ± 2.4	2.78	5.72	2.4
FS1	3.0	2.4	20.1	64 ± 17	3.5 ± 2.0	1.65	1.75	2.6
FS2/3	6.5	7.0	14.3	300 ± 75	1.7 ± 0.95	34.7	18.6	3.9

Note. Only the component of the magnetic field on the plane of the sky has been considered for the λ and $P_{B_{POS}}$ measures.

turbulence from the scatter of the magnetic field orientation around a mean value. This scatter decreases in a stronger field such that:

$$B_{POS} = Q\sqrt{4\pi\rho}\frac{\delta V}{\delta\phi} \approx 9.3\sqrt{n(H_2)}\frac{\Delta V}{\delta\phi}, \quad (4)$$

where Q is a factor of the order of unity, here taken to be 0.5, ρ is the density, δV is the turbulent velocity dispersion, and $\delta\phi$ is the magnetic field position-angle dispersion. In the rightmost expression, $n(H_2)$ is a number density of hydrogen molecules in cm^{-3}, ΔV is an FWHM linewidth in kilometers per second, and $\delta\phi$ is the magnetic field position-angle dispersion in degrees, which results in a field strength measured in microgauss (e.g., Ostriker et al. 2001; Crutcher et al. 2004).

Table 2 lists our estimates for the magnetic field strength within each of the filaments in Serpens Main, using the DCF technique. The number densities are calculated from the mean column density of the individual filaments (Figure 5) divided by the filament widths listed in Table 1 (Lee et al. 2014), assuming no additional line-of-sight modification. Nonthermal velocity dispersions are adopted from spectral-line observations of N_2H^+ made by Lee et al. (2014), also as shown in Table 1. The model of ordered background magnetic field morphology that is required in order to accurately calculate a field dispersion is obtained from the Stokes Q and U maps smoothed to a resolution of 28″, which is equivalent to the two-times-larger beam. This 28″ resolution corresponds to 0.056 pc at the target distance, which is reasonable for the background ordered fields of filamentary structures with a width ≈0.03–0.05 pc. The field dispersions we measure are distributed from 14.°3 to 29.°4 and are plotted in Figure 8. These values provide magnetic field strengths on the plane of the sky ranging from 64 to 300 μG. When estimating the uncertainty on the magnetic field strength, we assume a 50% error for the densities and use the fitting error for the field position-angle dispersion. Combined, this results in 25%–42% uncertainty in magnetic field strength.

We also estimate the mass-to-flux ratios (λ) with respect to their critical values, which measure whether the structures are supported by magnetic fields or if they are expected to gravitationally contract:

$$\lambda = \frac{(M/\Phi)_{obs}}{(M/\Phi)_{crit}} = 7.6 \times 10^{-21}\frac{N(H_2)}{B}, \quad (5)$$

where $N(H_2)$ is the column density of hydrogen molecules in units of cm^{-2}, and B is the magnetic field strength in microgauss (e.g., Crutcher et al. 2004). Regions with $\lambda > 1$ can gravitationally contract. The uncertainties on λ are calculated as $\sigma_\lambda = \sqrt{(\sigma_N/N(H_2))^2 + (\sigma_B/B)^2}$, so they are in the range of 56%–65% when adopting the uncertainties used in the previous

paragraph. Note that this measure of uncertainty provides only a rough estimate, as we assume Gaussian distributions for the uncertainties on column density and the magnetic field strength, which may in fact not be independent of each other. Table 2 shows the λ values for each filament. Note that the values are based on only the projected magnetic field component. Therefore, depending on the three-dimensional (3D) orientation of the magnetic fields, λ may be smaller. We also compare the magnetic field energy density (P_B) and the turbulence energy density ($P_{\rm turb}$) of individual filaments, which are, respectively, calculated as

$$P_B = \frac{B^2}{8\pi}, \tag{6}$$

$$P_{\rm turb} = \frac{3}{2}\rho\sigma_{\rm nt}^2. \tag{7}$$

Here $\sigma_{\rm nt}$ is nonthermal velocity dispersion. Finally, the last column of Table 2 presents the ratio of mass-per-length to the critical value for a cylindrical structure ignoring magnetic fields, as reported by Lee et al. (2014; our Table 1). Values greater than 1 indicate that such a structure can gravitationally contract.

From these measurements, we classify the filaments into three groups: {FN1, FC1}, {FC2, FS1}, and {FS2/3}. In FN1 and FC1, the magnetic and turbulent energy densities are comparable to each other. Note that λ and the magnetic field energy density are calculated from partial components of the fields, specifically the component projected on the plane of the sky. When the 3D orientation of the structure is considered, the total magnetic field may be significantly larger. For example, if the 3D magnetic field strength is larger than the plane-of-the-sky component by a factor of 2, λ and the magnetic field energy density become halved and quadrupled, respectively. The FN1 and FC1 filaments both have λ and line mass ratios either smaller than or close to 1, which suggests that these filaments may not be able to contract gravitationally. It is noteworthy that these filaments have no star formation activity (no YSOs) and that they have large velocity gradients, of 3–5 km s^{-1} pc^{-1} (Table 1).

FC2 and FS1 also have magnetic field and turbulence energy densities comparable to one another. These filaments, however, have both λ and mass ratios larger than two, which suggests that they are likely to gravitationally contract. Indeed, there are YSOs found in FS1 (Lee et al. 2014). In the FC2 filament, there are no YSOs found, but it seems to be gravitationally unstable. If FC2 is in fact not gravitationally unstable, our results suggest that significant magnetic support would be required in order to stabilize the structure. For such support to exist, based on the plane-of-sky values of λ that we measure, the filament would require a significant fraction of its magnetic field to be directed along the line of sight.

Lastly, FS2/3, which is the combined region of FS2 and FS3, has the strongest magnetic field among the filaments. The magnetic field energy density is also twice as large as the turbulence energy density. Therefore, magnetic fields dominate over turbulence in this combined structure. Even with the relatively strong magnetic field compared to turbulence, the filaments have $\lambda > 1$ and evidence for YSOs, indicating that the regions remain gravitationally unstable.

5. Conclusions

We have studied the physical conditions associated with the magnetic field within the Serpens Main molecular cloud using JCMT POL-2 850 μm polarimetric data, with a 14″ resolution, taken as part of the BISTRO survey. Serpens Main consists of two subclusters, containing a total of six filamentary structures (FN1, FC1/2, FS1/2/3) encompassing a variety of physical properties.

The most common direction of the linear polarization in Serpens Main, on ~6000 au scales, has P.A. = 4°.5, which suggests that the overall magnetic fields are east–west on the plane of sky. The submillimeter polarization fraction across Serpens Main decreases with the total intensity as $p \propto I^{-0.634}$. A power-law index shallower than −1 implies that the polarized emission is not limited to the surface of the molecular cloud. The observed polarization fraction decrease can be understood as being the result of weakening alignment mechanisms and/or magnetic field variations as a function of increasing density within the cloud.

Using the HRO technique, we find that the magnetic fields are predominantly perpendicular to the filamentary structures for all filaments except FN1 and FC1, which are the least dense and have no YSOs. The field orientation transitions from parallel ($\xi > 0$) to perpendicular ($\xi < 0$) with respect to the filaments when $N_{\rm H_2} \approx 0.93 \times 10^{22}$ cm^{-2}. We extend the typical HRO analysis to explore the magnetic field within the entire cloud and find that ξ again increases at $N_{\rm H_2} \approx 4.6 \times 10^{22}$ cm^{-2}, which can be understood as the result of a density gradient along elongated structures becoming significant (e.g., via core formation). Furthermore, ξ again becomes negative at $N_{\rm H_2} \approx 16 \times 10^{22}$ cm^{-2}, which is interpreted as resulting from the magnetic field being dragged along with increasing density.

We estimate magnetic field strengths in the filaments ranging from $B_{\rm POS} = 60$–300 μG, using the DCF method. The magnetic field energy density is comparable to or larger than the turbulent energy in all filaments. The starless filaments FN1 and FC1 might be supported by either the magnetic field or turbulence, while the other filaments appear to be gravitationally unstable. The combined filaments FS2/3, with the strongest magnetic field, also seem to be gravitationally unstable.

We are grateful to the anonymous referee for helpful comments. W.K. is supported by the New Faculty Startup Fund from Seoul National University and by the National Research Foundation of Korea (NRF) grant funded by the Korean government (MSIT) (NRF-2021R1F1A1061794). K.P. is a Royal Society University Research Fellow, supported by grant No. URF\ R1\ 211322. D.J. is supported by NRC Canada and by an NSERC Discovery grant. C.L.H.H. acknowledges support from the NAOJ Fellowship and JSPS KAKENHI grants 18K13586 and 20K14527. M.T. is supported by JSPS KAKENHI grant Nos. 18H05442, 15H02063, and 22000005. K.Q. is partially supported by National Key R&D Program of China No. 2017YFA0402600, and acknowledges the National Natural Science Foundation of China (NSFC) grant U1731237. C.W.L. is supported by the Basic Science Research Program through the NRF funded by the Ministry of Education, Science and Technology (NRF-2019R1A2C1010851). C.E. acknowledges the financial support from grant RJF/2020/000071 as a part of Ramanujan Fellowship awarded by Science and Engineering Research Board (SERB), Department of Science and Technology (DST), Govt. of India. L.F. and F.K. acknowledge the support of the Ministry of Science and

Technology of Taiwan under grant MOST107-2119-M-001-031-MY3 and Academia Sinica under grant AS-IA-106-M03. A.S. was supported by the National Science Foundation under grant AST-1715876. G.P. is supported by the Basic Science Research Program through the National Research Foundation of Korea (NRF) funded by the Ministry of Education (NRF-2020R1A6A3A01100208). T.H. is supported by the National Research Foundation of Korea (NRF) grant funded by the Korean government (MSIT) through the Mid-career Research Program (2019R1A2C1087045). S.-P.L. acknowledges grants from the Ministry of Science and Technology of Taiwan 106-2119-M-007-021-MY3 and 109-2112-M-007-010-MY3. Y.-W.T. was supported by the grant MOST 108-2112-M-001-004-MY2.

This study is part of the JCMT Large Program BISTRO observed under the project code M16AL004. The James Clerk Maxwell Telescope is operated by the East Asian Observatory on behalf of The National Astronomical Observatory of Japan; Academia Sinica Institute of Astronomy and Astrophysics; the Korea Astronomy and Space Science Institute; and Center for Astronomical Mega-Science (as well as the National Key R&D Program of China with No. 2017YFA0402700). Additional funding support is provided by the Science and Technology Facilities Council of the United Kingdom and participating universities and organizations in the United Kingdom and Canada. Additional funds for the construction of SCUBA-2 and POL-2 were provided by the Canada Foundation for Innovation. The authors wish to recognize and acknowledge the very significant cultural role and reverence that the summit of Maunakea has always had within the indigenous Hawaiian community. We are most fortunate to have the opportunity to conduct observations from this mountain.

Facility: JCMT

ORCID iDs

Woojin Kwon https://orcid.org/0000-0003-4022-4132
Kate Pattle https://orcid.org/0000-0002-8557-3582
Sarah Sadavoy https://orcid.org/0000-0001-7474-6874
Charles L. H. Hull https://orcid.org/0000-0002-8975-7573
Doug Johnstone https://orcid.org/0000-0002-6773-459X
Derek Ward-Thompson https://orcid.org/0000-0003-1140-2761
James Di Francesco https://orcid.org/0000-0002-9289-2450
Patrick M. Koch https://orcid.org/0000-0003-2777-5861
Ray Furuya https://orcid.org/0000-0003-0646-8782
Yasuo Doi https://orcid.org/0000-0001-8746-6548
Valentin J. M. Le Gouellec https://orcid.org/0000-0002-5714-799X
Jihye Hwang https://orcid.org/0000-0001-7866-2686
A-Ran Lyo https://orcid.org/0000-0002-9907-8427
Archana Soam https://orcid.org/0000-0002-6386-2906
Xindi Tang https://orcid.org/0000-0002-4154-4309
Thiem Hoang https://orcid.org/0000-0003-2017-0982
Florian Kirchschlager https://orcid.org/0000-0002-3036-0184
Lapo Fanciullo https://orcid.org/0000-0001-9930-9240
Kyoung Hee Kim https://orcid.org/0000-0001-9597-7196
Takashi Onaka https://orcid.org/0000-0002-8234-6747
Vera Könyves https://orcid.org/0000-0002-3746-1498
Ji-hyun Kang https://orcid.org/0000-0001-7379-6263
Motohide Tamura https://orcid.org/0000-0002-6510-0681
Pierre Bastien https://orcid.org/0000-0002-0794-3859
Shih-Ping Lai https://orcid.org/0000-0001-5522-486X
Keping Qiu https://orcid.org/0000-0002-5093-5088
Doris Arzoumanian https://orcid.org/0000-0002-1959-7201
Tyler L. Bourke https://orcid.org/0000-0001-7491-0048
Do-Young Byun https://orcid.org/0000-0003-1157-4109
Wen Ping Chen https://orcid.org/0000-0002-5519-0628
Huei-Ru Vivien Chen https://orcid.org/0000-0002-9774-1846
Zhiwei Chen https://orcid.org/0000-0003-0849-0692
Tao-Chung Ching (慶道沖) https://orcid.org/0000-0001-8516-2532
Jungyeon Cho https://orcid.org/0000-0003-1725-4376
Antonio Chrysostomou https://orcid.org/0000-0002-9583-8644
Eun Jung Chung https://orcid.org/0000-0003-0014-1527
Simon Coudé https://orcid.org/0000-0002-0859-0805
Hao-Yuan Duan https://orcid.org/0000-0002-7022-4742
David Eden https://orcid.org/0000-0002-5881-3229
Laura M. Fissel https://orcid.org/0000-0002-4666-609X
Erica Franzmann https://orcid.org/0000-0003-2142-0357
Per Friberg https://orcid.org/0000-0002-8010-8454
Rachel Friesen https://orcid.org/0000-0001-7594-8128
Gary Fuller https://orcid.org/0000-0001-8509-1818
Tim Gledhill https://orcid.org/0000-0002-2859-4600
Sarah Graves https://orcid.org/0000-0001-9361-5781
Jane Greaves https://orcid.org/0000-0002-3133-413X
Qilao Gu https://orcid.org/0000-0002-2826-1902
Jennifer Hatchell https://orcid.org/0000-0002-4870-2760
Martin Houde https://orcid.org/0000-0003-4420-8674
Tsuyoshi Inoue https://orcid.org/0000-0002-7935-8771
Shu-ichiro Inutsuka https://orcid.org/0000-0003-4366-6518
Kazunari Iwasaki https://orcid.org/0000-0002-2707-7548
Miju Kang https://orcid.org/0000-0002-5016-050X
Akimasa Kataoka https://orcid.org/0000-0003-4562-4119
Koji Kawabata https://orcid.org/0000-0001-6099-9539
Francisca Kemper https://orcid.org/0000-0003-2743-8240
Kee-Tae Kim https://orcid.org/0000-0003-2412-7092
Gwanjeong Kim https://orcid.org/0000-0003-2011-8172
Mi-Ryang Kim https://orcid.org/0000-0002-1408-7747
Shinyoung Kim https://orcid.org/0000-0001-9333-5608
Jongsoo Kim https://orcid.org/0000-0002-1229-0426
Jason Kirk https://orcid.org/0000-0002-4552-7477
Masato I. N. Kobayashi https://orcid.org/0000-0003-3990-1204
Takayoshi Kusune https://orcid.org/0000-0002-9218-9319
Jungmi Kwon https://orcid.org/0000-0003-2815-7774
Kevin Lacaille https://orcid.org/0000-0001-9870-5663
Chi-Yan Law https://orcid.org/0000-0003-1964-970X
Chin-Fei Lee https://orcid.org/0000-0002-3024-5864
Yong-Hee Lee https://orcid.org/0000-0001-6047-701X
Hyeseung Lee https://orcid.org/0000-0003-3465-3213
Jeong-Eun Lee https://orcid.org/0000-0003-3119-2087
Sang-Sung Lee https://orcid.org/0000-0002-6269-594X
Di Li https://orcid.org/0000-0003-3010-7661
Hua-bai Li https://orcid.org/0000-0003-2641-9240
Sheng-Jun Lin (林聖鈞) https://orcid.org/0000-0002-6868-4483
Sheng-Yuan Liu https://orcid.org/0000-0003-4603-7119
Junhao Liu (刘峻豪) https://orcid.org/0000-0002-4774-2998
Xing Lu https://orcid.org/0000-0003-2619-9305

Steve Mairs https://orcid.org/0000-0002-6956-0730
Masafumi Matsumura (松村雅文) https://orcid.org/0000-0002-6906-0103
Brenda Matthews https://orcid.org/0000-0003-3017-9577
Gerald Moriarty-Schieven https://orcid.org/0000-0002-0393-7822
Tetsuya Nagata https://orcid.org/0000-0001-9264-9015
Fumitaka Nakamura https://orcid.org/0000-0001-5431-2294
Nagayoshi Ohashi https://orcid.org/0000-0003-0998-5064
Geumsook Park https://orcid.org/0000-0001-8467-3736
Harriet Parsons https://orcid.org/0000-0002-6327-3423
Tae-Soo Pyo https://orcid.org/0000-0002-3273-0804
Lei Qian https://orcid.org/0000-0003-0597-0957
Ramprasad Rao https://orcid.org/0000-0002-1407-7944
Jonathan Rawlings https://orcid.org/0000-0001-5560-1303
Mark G. Rawlings https://orcid.org/0000-0002-6529-202X
John Richer https://orcid.org/0000-0002-9693-6860
Andrew Rigby https://orcid.org/0000-0002-3351-2200
Giorgio Savini https://orcid.org/0000-0003-4449-9416
Yoshito Shimajiri https://orcid.org/0000-0001-9368-3143
Hiroko Shinnaga https://orcid.org/0000-0001-9407-6775
Mehrnoosh Tahani https://orcid.org/0000-0001-8749-1436
Ya-Wen Tang https://orcid.org/0000-0002-0675-276X
Kohji Tomisaka https://orcid.org/0000-0003-2726-0892
Le Ngoc Tram https://orcid.org/0000-0002-6488-8227
Serena Viti https://orcid.org/0000-0001-8504-8844
Hongchi Wang https://orcid.org/0000-0003-0746-7968
Jia-Wei Wang https://orcid.org/0000-0002-6668-974X
Jintai Wu https://orcid.org/0000-0001-7276-3590
Hsi-Wei Yen https://orcid.org/0000-0003-1412-893X
Hyunju Yoo https://orcid.org/0000-0002-8578-1728
Hyeong-Sik Yun https://orcid.org/0000-0001-6842-1555
Yapeng Zhang https://orcid.org/0000-0002-5102-2096
Chuan-Peng Zhang https://orcid.org/0000-0002-4428-3183
Philippe André https://orcid.org/0000-0002-3413-2293

References

Andersson, B. G., Lazarian, A., & Vaillancourt, J. E. 2015, ARA&A, 53, 501
Arzoumanian, D., Furuya, R., Hasegawa, T., et al. 2021, A&A, 647, A78
Bich Ngoc, N., Diep, P. N., Parsons, H., et al. 2021, ApJ, 908, 10
Chandrasekhar, S., & Fermi, E. 1953, ApJ, 118, 113
Chapin, E. L., Berry, D. S., Gibb, A. G., et al. 2013, MNRAS, 430, 2545
Coudé, S., Bastien, P., Houde, M., et al. 2019, ApJ, 877, 88
Cox, E. G., Harris, R. J., Looney, L. W., et al. 2018, ApJ, 855, 92
Crutcher, R. M., Nutter, D. J., Ward-Thompson, D., & Kirk, J. M. 2004, ApJ, 600, 279
Currie, M. J., Berry, D. S., Jenness, T., et al. 2014, in ASP Conf. Ser. 485, Astronomical Data Analysis Software and Systems XXIII, ed. N. Manset & P. Forshay (San Francisco, CA: ASP), 391
Davis, L. 1951, PhRv, 81, 890
Dempsey, J. T., Friberg, P., Jenness, T., et al. 2013, MNRAS, 430, 2534
Doi, Y., Hasegawa, T., Furuya, R. S., et al. 2020, ApJ, 899, 28
Doi, Y., Tomisaka, K., Hasegawa, T., et al. 2021, ApJL, 923, L9
Dzib, S., Loinard, L., Mioduszewski, A. J., et al. 2010, ApJ, 718, 610
Eswaraiah, C., Li, D., Furuya, R. S., et al. 2021, ApJL, 912, L27
Evans, N. J. I., Dunham, M. M., Jørgensen, J. K., et al. 2009, ApJS, 181, 321
Friberg, P., Bastien, P., Berry, D., et al. 2016, Proc. SPIE, 9914, 991403
Girart, J. M., Rao, R., & Marrone, D. P. 2006, Sci, 313, 812
Graves, S. F., Richer, J. S., Buckle, J. V., et al. 2010, MNRAS, 409, 1412
Güver, T., & Özel, F. 2009, MNRAS, 400, 2050
Harvey, P., Merín, B., Huard, T. L., et al. 2007, ApJ, 663, 1149
Hennebelle, P., & Inutsuka, S.-i 2019, FrASS, 6, 5
Herczeg, G. J., Kuhn, M. A., Zhou, X., et al. 2019, ApJ, 878, 111
Hoang, T., Tram, L. N., Lee, H., Diep, P. N., & Bich Ngoc, N. 2021, ApJ, 908, 218
Holland, W. S., Bintley, D., Chapin, E. L., et al. 2013, MNRAS, 430, 2513
Hull, C. L. H., Plambeck, R. L., Bolatto, A. D., et al. 2013, ApJ, 768, 159
Hull, C. L. H., Plambeck, R. L., Kwon, W., et al. 2014, ApJS, 213, 13
Hull, C. L. H., Girart, J. M., Tychoniec, Ł., et al. 2017, ApJ, 847, 92
Hwang, J., Kim, J., Pattle, K., et al. 2021, ApJ, 913, 85
Jones, T. J., Bagley, M., Krejny, M., Andersson, B. G., & Bastien, P. 2015, AJ, 149, 31
Kauffmann, J., Bertoldi, F., Bourke, T. L., Evans, N. J., & Lee, C. W. 2008, A&A, 487, 993
Könyves, V., Ward-Thompson, D., Pattle, K., et al. 2021, ApJ, 913, 57
Kwon, J., Doi, Y., Tamura, M., et al. 2018, ApJ, 859, 4
Kwon, W., Stephens, I. W., Tobin, J. J., et al. 2019, ApJ, 879, 25
Lazarian, A., & Hoang, T. 2007, MNRAS, 378, 910
Le Gouellec, V. J. M., Hull, C. L. H., Maury, A. J., et al. 2019, ApJ, 885, 106
Le Gouellec, V. J. M., Maury, A. J., Guillet, V., et al. 2020, A&A, 644, A11
Lee, C.-F., Li, Z.-Y., Ching, T.-C., Lai, S.-P., & Yang, H. 2018, ApJ, 854, 56
Lee, K. I., Fernández-López, M., Storm, S., et al. 2014, ApJ, 797, 76
Li, H.-b., Goodman, A., Sridharan, T. K., et al. 2014, in Protostars and Planets VI, ed. H. Beuther et al. (Tucson, AZ: Univ. Arizona Press), 101
Liu, J., Qiu, K., Berry, D., et al. 2019, ApJ, 877, 43
Lyo, A.-R., Kim, J., Sadavoy, S., et al. 2021, ApJ, 918, 85
Matthews, B. C., McPhee, C. A., Fissel, L. M., & Curran, R. L. 2009, ApJS, 182, 143
Maury, A. J., Girart, J. M., Zhang, Q., et al. 2018, MNRAS, 477, 2760
Mouschovias, T. C. 1979, ApJ, 228, 475
Ostriker, E. C., Stone, J. M., & Gammie, C. F. 2001, ApJ, 546, 980
Ostriker, J. 1964, ApJ, 140, 1056
Palmeirim, P., André, P., Kirk, J., et al. 2013, A&A, 550, A38
Pattle, K., Ward-Thompson, D., Berry, D., et al. 2017, ApJ, 846, 122
Pattle, K., Ward-Thompson, D., Hasegawa, T., et al. 2018, ApJL, 860, L6
Pattle, K., Lai, S.-P., Hasegawa, T., et al. 2019, ApJ, 880, 27
Pattle, K., Lai, S.-P., Di Francesco, J., et al. 2021a, ApJ, 907, 88
Pattle, K., Lai, S.-P., Wright, M., et al. 2021b, MNRAS, 503, 3414
Pillai, T. G. S., Clemens, D. P., Reissl, S., et al. 2020, NatAS, 4, 1195
Planck Collaboration, Ade, P. A. R., Aghanim, N., et al. 2016, A&A, 586, A138
Planck Collaboration, Aghanim, N., Akrami, Y., et al. 2020, A&A, 641, A12
Rosolowsky, E. W., Pineda, J. E., Kauffmann, J., & Goodman, A. A. 2008, ApJ, 679, 1338
Sadavoy, S. I., Myers, P. C., Stephens, I. W., et al. 2018, ApJ, 869, 115
Sadavoy, S. I., Stephens, I. W., Myers, P. C., et al. 2019, ApJS, 245, 2
Shirley, Y. L. 2015, PASP, 127, 299
Soam, A., Pattle, K., Ward-Thompson, D., et al. 2018, ApJ, 861, 65
Soler, J. D., Hennebelle, P., Martin, P. G., et al. 2013, ApJ, 774, 128
Stephens, I. W., Looney, L. W., Kwon, W., et al. 2013, ApJL, 769, L15
Sugitani, K., Nakamura, F., Tamura, M., et al. 2010, ApJ, 716, 299
Wang, J.-W., Koch, P. M., Galván-Madrid, R., et al. 2020, ApJ, 905, 158
Wang, J.-W., Lai, S.-P., Eswaraiah, C., et al. 2019, ApJ, 876, 42
Ward-Thompson, D., Pattle, K., Bastien, P., et al. 2017, ApJ, 842, 66
Winston, E., Megeath, S. T., Wolk, S. J., et al. 2007, ApJ, 669, 493
Yen, H.-W., Koch, P. M., Hull, C. L. H., et al. 2021, ApJ, 907, 33